

## Topological Corner Modes Induced by Dirac Vortices in Arbitrary Geometry

Xiaoxiao Wu,<sup>1</sup> Yan Meng,<sup>2</sup> Yiran Hao,<sup>2</sup> Ruo-Yang Zhang,<sup>2</sup> Jensen Li<sup>1,2,\*</sup> and Xiang Zhang<sup>1,†</sup>

<sup>1</sup>*Faculties of Sciences and Engineering, The University of Hong Kong, Hong Kong, China*

<sup>2</sup>*Department of Physics, The Hong Kong University of Science and Technology, Clear Water Bay, Kowloon, Hong Kong, China*

 (Received 8 September 2020; revised 2 May 2021; accepted 7 May 2021; published 4 June 2021)

Recently, higher-order topologies have been experimentally realized, featuring topological corner modes (TCMs) between adjacent topologically distinct domains. However, they have to comply with specific spatial symmetries of underlying lattices, hence their TCMs only emerge in very limited geometries, which significantly impedes generic applications. Here, we report a general scheme of inducing TCMs in arbitrary geometry based on Dirac vortices from aperiodic Kekulé modulations. The TCMs can now be constructed and experimentally observed in square and pentagonal domains incompatible with underlying triangular lattices. Such bound modes at arbitrary corners do not require their boundaries to run along particular lattice directions. Our scheme allows an arbitrary specification of numbers and positions of TCMs, which will be important for future on-chip topological circuits. Moreover, the general scheme developed here can be extended to other classical wave systems. Our findings reveal rich physics of aperiodic modulations, and advance applications of TCMs in realistic scenarios.

DOI: [10.1103/PhysRevLett.126.226802](https://doi.org/10.1103/PhysRevLett.126.226802)

Higher-order topological insulators (HOTIs) and associated topological corner modes (TCMs), originally proposed in quantum condensed matters [1–5], have been realized in various classical photonic [6–12] and phononic crystals [13–21]. It enables designs of TCMs in conjunction with previously found topological edge modes as cavities and waveguides, respectively, and allows their integration on the same device [22,23]. Generally, realizations of TCMs rely on specific topological properties of two meeting edges running along different crystal directions. Such a scheme only works for configurations that can preserve certain spatial symmetries of underlying lattices [17,24,25], giving rise to only a few choices for angles of corners, e.g.,  $90^\circ$  for square lattices [7,9,10,13,17,21] and  $60^\circ$  for kagome lattices [14,15]. Interestingly, there are also implementations using electronic circuit lattices [26–29]. In these cases, they are not used to control waves in a continuous medium, and the above discussed spatial symmetries translates into mathematical descriptions in terms of ports and network notations. Therefore, such strict limits definitely hinder the exploration of rich physics of HOTIs and their practical applications where complex geometries are often encountered.

Here, we adopt a different route toward realizing TCMs based on a band-folding mechanism through the enlargement of unit cells [30–32], and together with Dirac vortices using aperiodic Kekulé modulations [33–35], we are able to transcend geometric constraints on the corner and domain shapes in previous schemes intrinsically imposed by their own routes. Our scheme is experimentally realized using elastic phononic crystals. The mode profiles and robustness

of these TCMs in arbitrary polygonal domains are further confirmed by direct field mapping and their associated spatial Fourier spectra. This general scheme is not limited by specific materials and can be extended immediately to other classical wave systems, such as airborne acoustics, and photonics at optical frequencies. It leads to robust higher-order corner modes, which now can be designed in complex and compact geometries that will be useful for constructing topological integrated circuits and devices.

The initial phononic crystal is an elastic plate with slots arranged in a triangular lattice [Fig. 1(a)]. Each slot comprises three slits of the same shape [Fig. 1(b)]. Guaranteed by the  $C_{3v}$  symmetry, Dirac cones emerge at corners  $K_{\pm}$  of the first Brillouin zone (FBZ) when calculating bands with the primitive unit cell [36–38] [green shaded region in Fig. 1(a)]. Consequently, when considering an enlarged unit cell [red shaded region in Fig. 1(a)], the inequivalent Dirac cones at valleys  $K_{\pm}$  will be folded back [17,24,25], and a double Dirac cone emerges at  $\Gamma$  point, center of FBZ [Fig. 1(c)]. In each enlarged unit cell, there are three inequivalent slots labeled as  $A$ ,  $B_1$ , and  $B_2$ , respectively [Fig. 1(b)]. Once the slot widths ( $d_A$ ,  $d_{B_1}$ , and  $d_{B_2}$ ) are no longer identical, the double Dirac cone will be gapped, which can induce topological effects in the band gap [29–31]. Here, we impose a Kekulé modulation, which is manifested by alternating coupling strengths (an analog to single and double bonds in Kekulé structure of benzene) between neighboring sublattices [39–41], as the intervalley coupling. Hence, the slot centered at  $\mathbf{r} = (x, y)$  has width

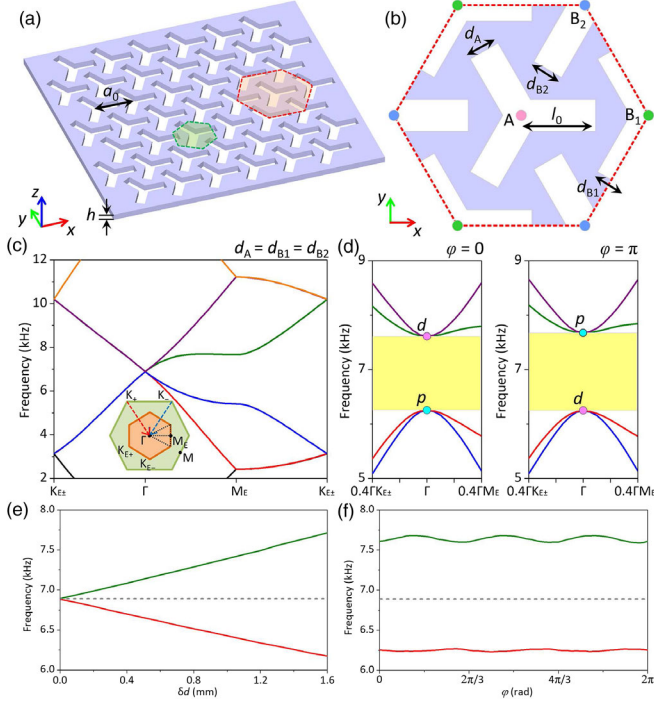


FIG. 1. Initial phononic crystal and homogeneous Kekulé modulation. (a) Schematic of initial phononic crystal, which is a thin elastic plate with a triangular lattice of depicted identical slots. Green (red) shaded region denotes a primitive (enlarged) unit cell. (b) Schematic of enlarged unit cell. Initially, slot length  $l_0 = 7.0$  mm, and uniform slot widths  $d_A = d_{B1} = d_{B2} = d_0 = 3.0$  mm. Other geometric parameters  $a_0 = 12.0$  mm,  $h = 2.0$  mm. (c) Band structure of flexural ( $A_0$ ) modes calculated using enlarged unit cell, with unperturbed uniform slot width  $d_0$ . Inset: two inequivalent Dirac cones at  $K_+$  and  $K_-$  valleys folded back into  $\Gamma$  point. (d) Band structures around  $\Gamma$  point when we apply a homogeneous Kekulé modulation with  $\varphi = 0$  and  $\pi$ , respectively. The modulation strength  $\delta d = 1.4$  mm. The frequency order of dipolelike ( $p$ ) and quadrupolelike ( $d$ ) modes suggests that  $\varphi = 0$  ( $\varphi = \pi$ ) corresponds to an ordinary insulator (topological insulator), or OI (TI). Yellow shaded regions denote the common band gap. (e),(f) Size of the band gap with respect to modulation strength  $\delta d$  (e) and phase  $\varphi$  (f).

$d(\mathbf{r}) = d_0 + \delta d \cos(\mathbf{K} \cdot \mathbf{r} + \varphi)$ , where  $d_0$  is the initial slot width,  $\mathbf{K} = \mathbf{K}_+ - \mathbf{K}_-$  is called the Kekulé vector [33,34], and parameters  $\delta d$  and  $\varphi$  separately control strength and phase of the modulation. Straightforwardly, the slot widths are modulated to be  $d_A = d_0 + \delta d \cos \varphi$ ,  $d_{B1} = d_0 + \delta d \cos(\varphi + 2\pi/3)$ , and  $d_{B2} = d_0 + \delta d \cos(\varphi + 4\pi/3)$ . For demonstration, we calculate band structures when  $\varphi = 0$  and  $\pi$  [Fig. 1(d)]. According to frequency orders of the dipolelike ( $p$ ) and quadrupolelike ( $d$ ) modes,  $\varphi = 0$  corresponds to an ordinary insulator (OI) while  $\varphi = \pi$  corresponds to a topological insulator (TI), which hosts pseudospin-Hall edge states (see Supplemental Material, Note S4 [42–47]). Generally, this band topology is well described by the effective Hamiltonian (see Note S1 for details [42])

$$H(\mathbf{k}) = v_D \tau_0 \otimes (k_x \sigma_1 + k_y \sigma_2) + (m_1 \tau_1 - m_2 \tau_2) \otimes \sigma_3, \quad (1)$$

where  $\mathbf{k} = (k_x, k_y)$  is the Bloch wave vector,  $\sigma_i$  and  $\tau_i$  are identical ( $i = 0$ ) and Pauli ( $i = 1, 2, 3$ ) matrices. The parameter  $v_D$  represents Fermi velocity, while  $m_1$  and  $m_2$  stands for intervalley couplings introduced by the modulation, which can be grouped together as a Dirac mass  $m = m_1 + im_2$ . To the first order, it can be estimated [33] as  $m \propto e^{i\varphi} \delta d$ . Explicitly, the modulation opens a full band gap proportional to  $\delta d$  [Fig. 1(e)]. Implicitly, it introduces an additional phase  $\varphi$  in eigenmodes without significant impact on band gap [Fig. 1(f)]. Therefore, when becoming position dependent, the winding of modulation phase  $\varphi(\mathbf{r})$  naturally introduces phase vortices for the Dirac mass  $m(\mathbf{r})$ , referred to as Dirac vortices [48].

We now seek to realize TCMs for all corners of a square domain of the underlying triangular lattice, which disregards its specific spatial symmetries ( $C_3$  rotational symmetries here), the essential ingredient for TCMs in many previous HOTIs [5,14,15]. On a metastructure (the whole profile) of the initial phononic crystal, we apply an aperiodic Kekulé modulation [Fig. 2(a)]

$$d(\mathbf{r}) = d_0 + \delta d \cos[\mathbf{K} \cdot \mathbf{r} + \varphi(\mathbf{r})]. \quad (2)$$

The inhomogeneous phase  $\varphi(\mathbf{r})$  divides the modulated metastructure into two distinct domains. Though both domains are insulating phases, in the outer domain, we instruct  $\varphi(\mathbf{r}) = 0$ , hence it is simply an OI and only serves as cladding. On the contrary, in the inner domain, the phase field  $\varphi(\mathbf{r})$  needs to be aperiodic, thereby introducing a phase evolution on intervalley couplings. Here, we instruct a smooth profile  $\varphi(\mathbf{r})$  in the inner domain, chosen as a function which satisfies Laplace's equation (see Supplemental Material, Note S5 for other possible smooth phase profiles [42])

$$\Delta \varphi(\mathbf{r}) = 0, \quad (3)$$

with the boundary condition

$$\varphi(\mathbf{r})|_{\mathbf{r} \in E_j} = 2m_j \pi (m_j \in \mathbb{Z}), \quad (4)$$

at edge  $E_j$  ( $j = 1$  to 4) of the square, where  $\Delta$  is the two-dimensional Laplace operator, and  $m_j$  is an integer. The boundary conditions ensure continuous transitions between the inner domain and outer OIs [ $\varphi(\mathbf{r}) = 0$ ], and  $\varphi(\mathbf{r})$  is uniquely determined (see Supplemental Material, Note S7 [42]). The inner domain undergoing aperiodic Kekulé modulation is termed as a Kekulé modulated insulator (KMI). Because of a smooth profile in the inner domain, the KMI can only possess phase vortices around its corners. These phase vortices, characterized by winding numbers of phase  $\varphi(\mathbf{r})$  around the corners, then guarantee emergence

of TCMs by Jackiw-Rossi mechanism [33,48]. For a corner formed by edges  $E_i$  and  $E_j$ , the number of TCMs bound there is then  $N = |m_j - m_i|$ , which are dictated by the boundary conditions Eq. (4).

We hence consider alternating values of 0 and  $2\pi$  as boundary conditions of  $\varphi(\mathbf{r})$  for the four edges [Fig. 2(a)]. The metastructure is then designed according to Eq. (2) using discretized values of calculated  $\varphi(\mathbf{r})$ , which clearly demonstrates phase windings around the corners [Fig. 2(b) and inset]. With measured material parameters (see

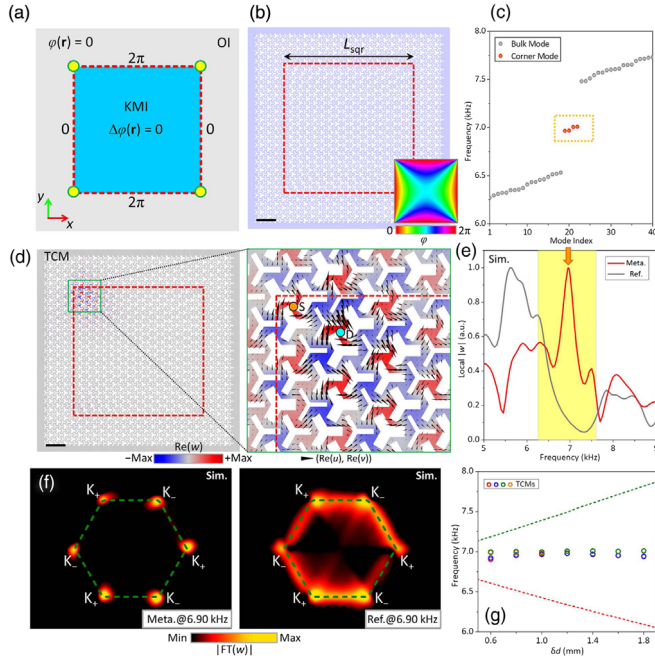


FIG. 2. Topological corner modes (TCMs) induced by Dirac vortices of aperiodic Kekulé modulation. (a) Schematic of designed metastructure with TCMs at four corners, a square domain (blue region) with aperiodic Kekulé modulation [ $\Delta\varphi(\mathbf{r}) = 0$ ] cladded by OIs [ $\varphi(\mathbf{r}) = 0$ , gray region]. The modulated domain is referred to as a Kekulé modulated insulator (KMI). Yellow dots represent Dirac vortices of  $2\pi$ -phase winding. (b) Generated pattern of metastructure in (a). The red dashed square ( $L_{\text{sqr}} = 320$  mm) delineate the OI and KMI. Inset: phase  $\varphi(\mathbf{r})$  of KMI. Black scale bar: 48 mm. (c) Calculated flexural eigenmodes of metastructure. (d) Field profile [ $\text{Re}(w)$ ] of one of the midgap modes. Selected area (green square) around the corner is enlarged, with black arrows denoting in-plane displacement [ $\text{Re}(u)$ ,  $\text{Re}(v)$ ]. Black scale bar: 48 mm. (e) Response spectra when exciting the metastructure and a reference structure. Positions of source point ( $S$ ) and detection point ( $D$ ) are depicted in (d). The orange arrow indicates the resonance at 6.97 kHz in the band gap (yellow shaded region). The reference structure only comprises OIs. Maximum of each spectrum is normalized to unity. (f) Fourier spectra [ $|\text{FT}(w)|$ ] of experimentally imaged field of metastructure (meta.) and reference structure (ref.) at 6.90 kHz. Green dashed hexagon: FBZ of primitive unit cell shown in Fig. 1(a). (g) Frequencies of the four TCMs versus modulation strength ( $\delta d$ ). Dashed lines indicate frequency range of the band gap.

Supplemental Material, Note S15 for detailed values [42]), 3D full-wave eigenmode simulations are performed and four midgap flexural modes emerge in the spectra of the metastructure [Fig. 2(c)]. The field profile of one of the midgap modes [Fig. 2(d)] confirms that it is indeed confined around the upper-left corner, and other midgap modes are confined around other corners (see Supplemental Material, Note S6 for all four TCM modes [42]). Its time-harmonic animation also confirms its localized and non-propagating feature (see Supplemental Material, Movie S1 [42]). We also examine the local response at upper-left corner [Fig. 2(e)]. It clearly demonstrates a resonance peak at 6.97 kHz around middle of the band gap, though not very sharp ( $Q \approx 26.8$ ) due to elastic loss included in simulations (see Supplemental Material, Note S15 [42]). We perform spatial Fourier transforms (SFTs) on the numerically excited field [36,37], and the Fourier spectra confirm that only regions around  $K_{\pm}$  valleys are occupied by the mode, which is a key signature of its topological origin from intervalley couplings. For comparison, we can see the Fourier spectra of the reference structure shows no such concentrated occupation in reciprocal space [Fig. 2(f)]. The frequencies of the four midgap TCMs are also insensitive to modulation strength [Fig. 2(g)]. The small frequency split of four TCMs is mainly owing to the incompatibility between rotational symmetries of the square KMI and the underlying triangular lattice.

For experimental corroboration, we perform field mapping to directly observe the TCMs. A sample of the designed metastructure [Fig. 2(b)] is 3D printed using stereolithography techniques [Fig. 3(a)]. We use piezoelectric speakers attached on the sample to excite flexural waves, and out-of-plane displacement is pointwise scanned by a scanning Doppler vibrometer [49] (see Supplemental Material, Note S15 for details [42]). The imaged field at 6.90 kHz (see Note S8 for fields at other frequencies [42]) indeed demonstrates good confinement around the corner [Fig. 3(b)]. To demonstrate strong field enhancement, a key feature of resonance modes, we also measure response spectra at the corner, edge, and bulk of the metastructure sample. Subsequently, a peak at 6.90 kHz emerges in the band gap when exciting at the corner, and it disappears when exciting at the edge and bulk [Fig. 3(c)]. For a definite confirmation, we perform SFTs on experimentally imaged displacement field, and the Fourier spectra confirm that the modes excited at the corner only occupy both valleys [Fig. 3(d)], in excellent agreement with simulations [Fig. 2(f)]. We then proceed to detect robustness of the resonance peak. By measuring the response spectra of similar samples but with different modulation strength  $\delta d$ , it is found that a resonance peak, from the same TCM, persists around the frequency 6.90 kHz in the enlarging band gaps [Fig. 3(e)].

Next, we demonstrate the emergence of TCMs in more general polygons with symmetries incompatible to the

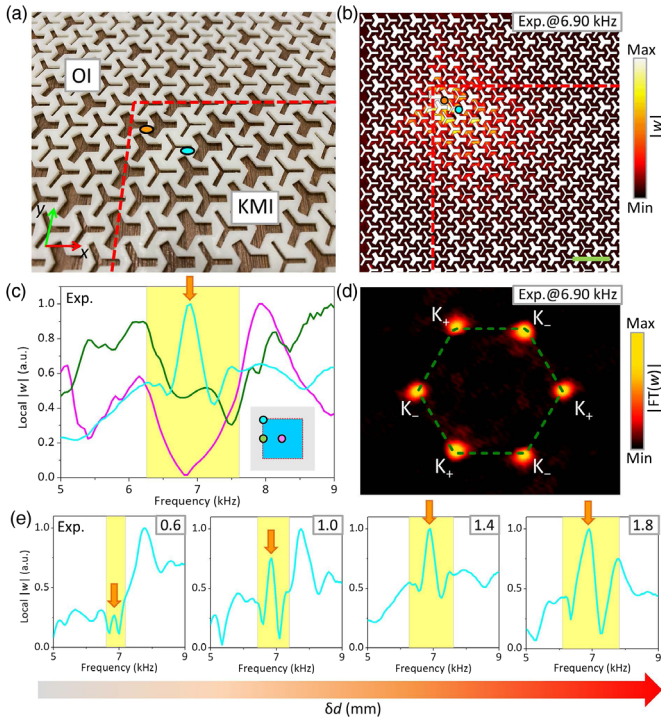


FIG. 3. Direct observations of TCMs and their robustness. (a) Photograph of the 3D-printed metastructure sample with a square domain of the KMI. Red dashed lines denote boundaries between the domains of OI and KMI. Orange (cyan) point denotes where we excite (detect) the out-of-plane displacement. (b) Experimentally imaged field of out-of-plane displacement ( $|w|$ ) at 6.90 kHz. Green scale bar: 36 mm. (c) Detected response spectra of the metastructure when exciting at the corner, edge, and bulk, respectively. The orange arrow indicates the resonance at 6.90 kHz. When measuring each spectrum, the displacement between the source and detection points is always  $\mathbf{r}_D - \mathbf{r}_S = (-3a_0/2, \sqrt{3}a_0/2)$ . Inset: colored dots indicate positions of detection points. (d) Fourier spectra ( $|FT(w)|$ ) of imaged fields of the metastructure. Green dashed hexagon: FBZ of primitive unit cell. (e) Detected response spectra at the upper-left corner for metastructure samples with varying strength  $\delta d$ . The resonance peak of the corner mode persists around 6.90 kHz in the broadening band gap (yellow shaded region), as indicated by orange arrows. The maximum of each spectrum is normalized to unity.

underlying triangular lattice. Here, we design a metastructure, which comprises a pentagonal KMI cladded by OIs [Fig. 4(a)]. For convenience, the metastructure is denoted as pentagon I, and the corners of the pentagonal KMI are denoted as  $A$  to  $E$ . The specified boundary conditions force the phase field  $\varphi(\mathbf{r})$  into winding around all corners except corner  $A$  [Fig. 4(b) and inset]. The calculated eigenfrequency spectrum shows that there are indeed four midgap corner modes for the metastructure [Fig. 4(c)], and their fields are confined around each corner except corner  $A$  where there is no phase winding (see Supplemental Material, Note S9 for fields of all four modes [42]). The

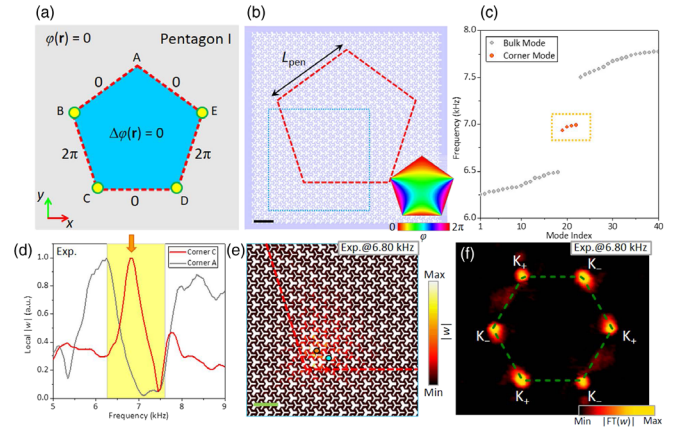


FIG. 4. Experimental observation of TCMs induced by Dirac vortices in pentagonal domains. (a) Schematic of a pentagonal KMI (blue region) cladded by OIs (gray region). The corners are labeled as  $A$  to  $E$  for convenience. Yellow dots represent Dirac vortices of  $2\pi$ -phase winding. (b) Pattern of the metastructure ( $L_{\text{pen}} = 200$  mm), denoted as pentagon I (pen. I). Blue dashed rectangle indicates the region imaged in experiments. Inset: distribution of phase  $\varphi(\mathbf{r})$  in the pentagonal domain. Black scale bar: 48 mm. (c) Calculated eigenmode spectra of the metastructure. (d) Local response spectra at corner  $A$  and corner  $C$ . Source and detection points around corner  $C$  are depicted in (e) as orange and cyan dots, respectively. (e) Imaged field map ( $|w|$ ) of the denoted region in (b) when exciting corner  $C$  at 6.80 kHz. Green scale bar: 36 mm. (f) Fourier spectra ( $|FT(w)|$ ) of the experimental field at 6.80 kHz. Green dashed hexagon: FBZ of primitive unit cell.

local response spectra are measured, and it is seen that a resonance peak emerges in the band gap for corner  $C$ , and no such resonance exists for corner  $A$  [Fig. 4(d)] when we excite around these corners. We have also experimentally imaged displacement field around corner  $C$  [Fig. 4(e)], and its Fourier spectra confirm its topological origin [Fig. 4(f)], showing occupation of both valleys similar to that of a square KMI [Fig. 3(d)]. Moreover, we note that it is also possible to induce multiple TCMs at a single corner by designing a higher phase winding around it (e.g.,  $4\pi$  to get two corner modes, see Supplemental Material, Note S10 [42]). Finally, we remark that TCMs can likewise emerge in heptagonal, octagonal, and irregular polygonal domains, even with curved boundaries (see Note S11 [42]). As their frequencies are only very slightly shifted for such a wide variety of shapes, the TCMs can offer a flexible and robust topological protection when designing topological circuits (see Notes S12 and S13 [42]).

In summary, the scheme of realizing TCMs in arbitrary polygonal domains opens a door for exploring topological matter arising from aperiodic modulations. The TCMs stemming from Dirac vortices instead of bulk-boundary correspondences is directly observed and its robustness is confirmed. The scheme no longer requires domains to maintain specific geometry for compatibility with their

underlying lattices to induce TCMs, and the number of TCMs for a corner is also customizable. As the emergence of these TCMs does not depend on specific material parameters, the scheme can be directly scaled for different working frequencies up to GHz, which is important for telecommunications and may lead to innovative integrated devices [18,32]. It is also obvious that although the scheme is proposed in the frame of a Hermitian theory, the induced TCMs are robust against non-Hermitian loss of the material. Thus, an interplay between the TCMs and non-Hermitian gain and loss may further advance their wave control applications [50–53], such as trapping, sensing, and lasing. Furthermore, the general scheme is also applicable for other classical systems (see Supplemental Material, Note S14 [42]), such as on-chip photonics, and may retrospectively inspire unprecedented topological matter in quantum condensed matters.

The work is supported by Hong Kong RGC Grant No. C6013-18G.

\*To whom correspondence should be addressed.  
jensenli@ust.hk

†To whom correspondence should be addressed.  
president@hku.hk

- [1] W. A. Benalcazar, B. A. Bernevig, and T. L. Hughes, *Science* **357**, 61 (2017).
- [2] J. Langbehn, Y. Peng, L. Trifunovic, F. von Oppen, and P. W. Brouwer, *Phys. Rev. Lett.* **119**, 246401 (2017).
- [3] Z. Song, Z. Fang, and C. Fang, *Phys. Rev. Lett.* **119**, 246402 (2017).
- [4] M. Ezawa, *Phys. Rev. Lett.* **120**, 026801 (2018).
- [5] S. Kempkes, M. Slot, J. van den Broeke, P. Capiod, W. Benalcazar, D. Vanmaekelbergh, D. Bercioux, I. Swart, and C. M. Smith, *Nat. Mater.* **18**, 1292 (2019).
- [6] B.-Y. Xie, G.-X. Su, H.-F. Wang, H. Su, X.-P. Shen, P. Zhan, M.-H. Lu, Z.-L. Wang, and Y.-F. Chen, *Phys. Rev. Lett.* **122**, 233903 (2019).
- [7] X.-D. Chen, W.-M. Deng, F.-L. Shi, F.-L. Zhao, M. Chen, and J.-W. Dong, *Phys. Rev. Lett.* **122**, 233902 (2019).
- [8] Y. Chen, Z.-K. Lin, H. Chen, and J.-H. Jiang, *Phys. Rev. B* **101**, 041109(R) (2020).
- [9] C. W. Peterson, W. A. Benalcazar, T. L. Hughes, and G. Bahl, *Nature (London)* **555**, 346 (2018).
- [10] S. Mittal, V. V. Orre, G. Zhu, M. A. Gorlach, A. Poddubny, and M. Hafezi, *Nat. Photonics* **13**, 692 (2019).
- [11] A. El Hassan, F. K. Kunst, A. Moritz, G. Andler, E. J. Bergholtz, and M. Bourennane, *Nat. Photonics* **13**, 697 (2019).
- [12] F. Zangeneh-Nejad and R. Fleury, *Phys. Rev. Lett.* **123**, 053902 (2019).
- [13] X. Zhang, H.-X. Wang, Z.-K. Lin, Y. Tian, B. Xie, M.-H. Lu, Y.-F. Chen, and J.-H. Jiang, *Nat. Phys.* **15**, 582 (2019).
- [14] X. Ni, M. Weiner, A. Alù, and A. B. Khanikaev, *Nat. Mater.* **18**, 113 (2019).
- [15] H. Xue, Y. Yang, F. Gao, Y. Chong, and B. Zhang, *Nat. Mater.* **18**, 108 (2019).
- [16] H. Fan, B. Xia, L. Tong, S. Zheng, and D. Yu, *Phys. Rev. Lett.* **122**, 204301 (2019).
- [17] X. Zhang, Z.-K. Lin, H.-X. Wang, Z. Xiong, Y. Tian, M.-H. Lu, Y.-F. Chen, and J.-H. Jiang, *Nat. Commun.* **11**, 65 (2020).
- [18] X. Zhang, B.-Y. Xie, H.-F. Wang, X. Xu, Y. Tian, J.-H. Jiang, M.-H. Lu, and Y.-F. Chen, *Nat. Commun.* **10**, 1 (2019).
- [19] H. Xue, Y. Yang, G. Liu, F. Gao, Y. Chong, and B. Zhang, *Phys. Rev. Lett.* **122**, 244301 (2019).
- [20] X. Ni, M. Li, M. Weiner, A. Alù, and A. B. Khanikaev, *Nat. Commun.* **11**, 2108 (2020).
- [21] Z. Zhang, H. Long, C. Liu, C. Shao, Y. Cheng, X. Liu, and J. Christensen, *Adv. Mater.* **31**, 1904682 (2019).
- [22] Y. Ota, F. Liu, R. Katsumi, K. Watanabe, K. Wakabayashi, Y. Arakawa, and S. Iwamoto, *Optica* **6**, 786 (2019).
- [23] X. Xie, W. Zhang, X. He, S. Wu, J. Dang, K. Peng, F. Song, L. Yang, H. Ni, and Z. Niu, C. Wang, K. Jin, X. Zhang, and X. Xu, *Laser Photonics Rev.* **14**, 1900425 (2020).
- [24] Y. Liu, Y. Wang, N. C. Hu, J. Y. Lin, C. H. Lee, and X. Zhang, *Phys. Rev. B* **102**, 035142 (2020).
- [25] X. Zhou, Z.-K. Lin, W. Lu, Y. Lai, B. Hou, and J.-H. Jiang, *Laser Photonics Rev.* **14**, 2000010 (2020).
- [26] S. Imhof, C. Berger, F. Bayer, J. Brehm, L. W. Molenkamp, T. Kiessling, F. Schindler, C. H. Lee, M. Greiter, T. Neupert, and R. Thomale, *Nat. Phys.* **14**, 925 (2018).
- [27] C. W. Peterson, W. A. Benalcazar, T. L. Hughes, and G. Bahl, *Nature (London)* **555**, 346 (2018).
- [28] M. Ezawa, *Phys. Rev. B* **98**, 201402(R) (2018).
- [29] F. Zangeneh-Nejad and R. Fleury, *Phys. Rev. Lett.* **123**, 053902 (2019).
- [30] L.-H. Wu and X. Hu, *Phys. Rev. Lett.* **114**, 223901 (2015).
- [31] Z. Zhang, Q. Wei, Y. Cheng, T. Zhang, D. Wu, and X. Liu, *Phys. Rev. Lett.* **118**, 084303 (2017).
- [32] S.-Y. Yu, C. He, Z. Wang, F.-K. Liu, X.-C. Sun, Z. Li, H.-Z. Lu, M.-H. Lu, X.-P. Liu, and Y.-F. Chen, *Nat. Commun.* **9**, 3072 (2018).
- [33] P. Gao, D. Torrent, F. Cervera, P. San-Jose, J. Sánchez-Dehesa, and J. Christensen, *Phys. Rev. Lett.* **123**, 196601 (2019).
- [34] E. Andrade, R. Carrillo-Bastos, and G. G. Naumis, *Phys. Rev. B* **99**, 035411 (2019).
- [35] C. Gutiérrez, C.-J. Kim, L. Brown, T. Schiros, D. Nordlund, E. B. Lochocki, K. M. Shen, J. Park, and A. N. Pasupathy, *Nat. Phys.* **12**, 950 (2016).
- [36] J. Lu, C. Qiu, M. Ke, and Z. Liu, *Phys. Rev. Lett.* **116**, 093901 (2016).
- [37] X. Wu, Y. Meng, J. Tian, Y. Huang, H. Xiang, D. Han, and W. Wen, *Nat. Commun.* **8**, 1304 (2017).
- [38] M. Yan, J. Lu, F. Li, W. Deng, X. Huang, J. Ma, and Z. Liu, *Nat. Mater.* **17**, 993 (2018).
- [39] C. Chamon, *Phys. Rev. B* **62**, 2806 (2000).
- [40] C.-Y. Hou, C. Chamon, and C. Mudry, *Phys. Rev. Lett.* **98**, 186809 (2007).
- [41] R. L. Frank and E. H. Lieb, *Phys. Rev. Lett.* **107**, 066801 (2011).
- [42] See Supplemental Material at <http://link.aps.org/supplemental/10.1103/PhysRevLett.126.226802>, which includes Refs. [43–47], for the derivation of effective Hamiltonian, band structure including decoupled modes, other possible smooth phase profiles, field maps at other

- corners and other frequencies, topological corner modes for more complex geometries, impact of corner shapes and integration with topological waveguides, direct application to other classical systems, and more details.
- [43] S. Barik, H. Miyake, W. DeGottardi, E. Waks, and M. Hafezi, *New J. Phys.* **18**, 113013 (2016).
- [44] O. Gamayun, V. Ostroukh, N. Gnezdilov, Í. Adagideli, and C. Beenakker, *New J. Phys.* **20**, 023016 (2018).
- [45] Y. Liu, Z. Liang, J. Zhu, L. Xia, O. Mondain-Monval, T. Brunet, A. Alù, and J. Li, *Phys. Rev. X* **9**, 011040 (2019).
- [46] W. Zhu and G. Ma, *Phys. Rev. B* **101**, 161301(R) (2020).
- [47] X. Zhang, L. Liu, M.-H. Lu, and Y.-F. Chen, *Phys. Rev. Lett.* **126**, 156401 (2021).
- [48] X. Gao, L. Yang, H. Lin, L. Zhang, J. Li, F. Bo, Z. Wang, and L. Lu, *Nat. Nanotechnol.* **15**, 1012 (2020).
- [49] Y. Liu, Z. Liang, F. Liu, O. Diba, A. Lamb, and J. Li, *Phys. Rev. Lett.* **119**, 034301 (2017).
- [50] M. Dubois, C. Shi, X. Zhu, Y. Wang, and X. Zhang, *Nat. Commun.* **8**, 14871 (2017).
- [51] Z. Zhang, M.R. López, Y. Cheng, X. Liu, and J. Christensen, *Phys. Rev. Lett.* **122**, 195501 (2019).
- [52] T. Liu, Y.-R. Zhang, Q. Ai, Z. Gong, K. Kawabata, M. Ueda, and F. Nori, *Phys. Rev. Lett.* **122**, 076801 (2019).
- [53] X.-W. Luo and C. Zhang, *Phys. Rev. Lett.* **123**, 073601 (2019).